Dynamic Rupture Modeling with a Rate and State Friction Law in a Discontinuous Galerkin Method

J. Tago[1,a,*], S.M. Day[2,b], V.M. Cruz-Atienza[3,c], and C. Villafuerte[3,d]

[1]Facultad de Ingeniería, Universidad Nacional Autónoma de México, Mexico City, Mexico

[2]Department of Geological Sciences, San Diego State University, San Diego, California, USA

[3]Instituto de Geofísica, Universidad Nacional Autónoma de México, Mexico City, Mexico

[a]https://orcid.org/0000-0002-8670-2024

[b]https://orcid.org/0000-0001-9924-9524

[c]https://orcid.org/0000-0001-7067-2636

[d]https://orcid.org/0000-0003-1539-3751

June 3, 2026

* Correspondence: tago@unam.mx

Resumen

La modelación de la dinámica de la ruptura sísmica ha demostrado ser una herramienta útil para comprender la física detrás de las distintas secuencias de deslizamiento inferidas a partir de observaciones. Sin embargo, modelar

Artículo en prensa / Article in press

la dinámica de los terremotos resulta un desafío debido al complejo comportamiento de la fricción durante la evolución de la ruptura. Implementamos una ley de fricción *rate & state* en DGCrack (Tago et al., 2012), un código numérico basado en el método de Galerkin discontinuo, con una estrategia de escalonamiento temporal inspirada en el trabajo de Rojas et al. (2009). Proponemos un flujo ad hoc sobre la falla en lugar del flujo *upwind* comúnmente utilizado en esquemas de Galerkin discontinuo (e.g. Zhang et al., 2023). Si bien este enfoque genera oscilaciones de alta frecuencia, las controlamos con un parámetro de amortiguamiento artificial sin comprometer el contenido espectral. Demostramos que DGCrack reproduce correctamente las formas de onda en la falla en comparación con otras estrategias numéricas de orden superior del estado del arte. Además, mostramos que el amortiguamiento artificial produce una dispersión y disipación numérica en nuestras simulaciones que resultan menores que las introducidas intrínsecamente por un flujo *upwind*.

Abstract

Earthquake rupture modeling has proven to be a useful tool to understand the physics behind different slip sequences inferred from observations. However, modeling earthquake dynamics is challenging due to the complex frictional behavior during the rupture evolution. We implement a rate-and-state friction law in DGCrack (Tago et al., 2012), a numerical code based on the discontinuous Galerkin method, with a time staggered strategy inspired by the work of Rojas et al. (2009). We propose an ad hoc flux along the fault instead of an upwind flux commonly used in discontinuous Galerkin schemes (e.g. Zhang et al., 2023). While this approach generates high-frequency oscillations, we control them through an artificial damping parameter without compromising spectral content. We show that DGCrack correctly reproduces fault waveforms compared with other higher-order state-of-the-art numerical strategies. Our simulations indicate that the artificial damping introduces numerical dispersion and dissipation that are actually smaller than those inherently introduced by an upwind flux.

Artículo en prensa / Article in press

Keywords: Discontinuous Galerkin method; Dynamic rupture; Rate and state friction law

1 Introduction

Understanding the rupture process of earthquakes has been one of the most challenging research topics of the seismological community. Dynamic rupture has been studied from complex experimental setups to computational modeling studies. Among the different friction laws that have been proposed, rate and state friction laws have proven particularly useful for reproducing both short- and long-term behavior of fault dynamics. These friction laws are favored by seismologists to model sequences of earthquakes and aseismic slip, as they can model not only the rupture but the healing process that follows (Erickson et al.,2020; Erickson et al.,2023).

Some of the earliest dynamic rupture numerical simulations were done with a boundary integral equation method (BIEM) (Das and Aki, 1977; Andrews, 1985). This approach has since been continuously developed due to its low computational cost and its suitability for simulating complex geometries (Lapusta et al., 2000; Ando and Kaneko, 2018; Qian et al., 2019; Aochi and Cruz-Atienza, 2025). However, BIEM is limited in its ability to handle heterogeneous media, prompting the development of full-domain discretization strategies. These include the finite difference method (FDM) (Andrews, 1976; Day, 1982; Madariaga et al., 1998; Cruz-Atienza and Virieux, 2004; Dalguer and Day, 2007; Moczo et al., 2007; Rojas et al., 2008; Kozdon et al., 2012, 2013), the finite volume method (FVM) (Benjemaa et al., 2007; Benjemaa et al., 2009), the finite element method (FEM) (Oglesby et al., 1998; Oglesby et al., 2000; Barall, 2009; Galis et al., 2010; Aagaard et al., 2013) and the spectral element method (SEM) (Ampuero, 2002; Kaneko et al., 2008; Galvez et al., 2014).

Among these, the staggered-grid finite difference method (FDM) has been widely adopted due to its computational efficiency and simplicity (Day et al., 2005; Dalguer and Day, 2007). Day and Ely (2002) described an artificial damping parameter for this strategy

Artículo en prensa / Article in press

to suppress spurious high-frequency oscillations (HFOs) due to the abrupt stress drops at the rupture front. This method has been highly successful because of its simple implementation and its ability to preserve the elastodynamic spectrum while selectively attenuating high-frequency oscillations (Day et al., 2005; Rojas et al., 2009).

The discontinuous Galerkin method (DGM) is particularly well suited for earthquake dynamics, as its solutions are inherently discontinuous at element boundaries. DGM combines the high-order accuracy of FEM (Zienkiewicz and Taylor,2005) with the flux strategies of FVM for handling discontinuous solutions (LeVeque, 2002). The first DGM for elastodynamics, using a linear slip weakening law, was introduced by Benjemaa et al. (2007) with constant basis functions in 2D, equivalent to FVM, and later extended to 3D (Benjemaa et al., 2009). De la Puente et al. (2009) developed ADER-DG, a high-order DGM combined with an arbitrarily higher-order derivatives (ADER) time integration scheme (Käser and Dumbser, 2006), for dynamic rupture with higher order approximations in space and time. However, high-order convergence was not achieved for dynamic rupture problems due to the nonlinearity of the fault rupture equations, as also reported by others (Day et al., 2005; Rojas et al., 2008). In ADER-DG, a modal basis is used, and the rupture discontinuity is resolved via an upwind flux (Godunov state). This strategy avoided the appearance of HFOs because of its dissipative nature (Hesthaven and Warburton, 2007). The 3D ADER-DG implementation was later completed by Pelties et al. (2012).

Another DGM approach, DGCrack, was simultaneously introduced by Tago et al. (2012) as a development of the GeoDG3D parallel code (Etienne et al., 2010). This nodal-basis method uses second order elements next to the fault discontinuity with an ad hoc fault flux. While DGCrack suffers from HFOs, its simplicity yields high computational efficiency and results comparable to those from third-order ADER-DG.

Rate and state friction laws were first coupled with DGM by Pelties et al. (2014), who also used an upwind flux to solve the Riemann problem. More recently, Zhang et al. (2023) introduced a Mixed-Flux-Based Nodal DGM that also solves the Riemann problem with an upwind flux on fault faces but with central fluxes along non-fault faces to mitigate

Artículo en prensa / Article in press

spatial spike oscillations (SSOs) caused by mesh asymmetry. They avoided central fluxes elsewhere due to potential HFOs, although these may have resulted from strong mesh coarsening. In fact, Etienne et al. (2010) demonstrated that dispersion remains controlled when the minimum wavelength resolution requirement, dependent on the approximation order, is satisfied.

In this study, we extend DGCrack to incorporate rate and state friction laws, drawing inspiration from Rojas et al. (2009) who proposed a time staggered for the friction coefficient computation. Our aim is to maintain the simplicity of second-order ad hoc fault fluxes while using energy-conserving central fluxes elsewhere. To suppress HFOs, we employ an artificial damping strategy following Day et al. (2005). This choice allow us to control energy dissipation, something not achievable with upwind fluxes, while also exploring an alternative approach that remains both simple and computationally efficient.

In the following sections, we first introduce the elastodynamic hyperbolic system together with the fault boundary conditions governed by rate-and-state friction. We then describe the discretization of these equations using a DGM, with particular emphasis on the computation of fault fluxes where frictional properties evolve dynamically. The Results section presents the verification of our implementation with the rate-and-state friction benchmark TPV104 from the Statewide California Earthquake Center (SCEC) (Harris et al.,2018). We begin by analyzing the role of artificial damping, followed by waveform comparisons with other state-of-the-art numerical approaches and an assessment of convergence under grid refinement. Finally, we conclude with a discussion of the advantages and limitations of our formulation.

2 Dynamic rupture equations

In dynamic rupture modeling, a friction law is applied along an inner boundary, the fault, embedded within an elastic medium. The following subsections present the governing continuum equations, the associated boundary conditions, and the formulation of the rate-and-state friction law.

Artículo en prensa / Article in press

2.1 Elastodynamics: First order hyperbolic system

The elastic wave propagation can be modelled with a velocity-stress formulation as a first-order hyperbolic system as:

$$\rho \partial_t \underline{v} = \sum_{\theta \in \{x,y,z\}} \partial_\theta \underline{\underline{M}}_\theta \underline{\sigma}, \tag{1}$$

$$\underline{\underline{\Lambda}} \partial_t \underline{\sigma} = \sum_{\theta \in \{x,y,z\}} \partial_\theta \underline{\underline{N}}_\theta \underline{v}, \tag{2}$$

where ∂_t and ∂_θ are the time and space derivatives for $\theta \in \{x, y, z\}$, ρ is the density, $\underline{\underline{\Lambda}} = \mathrm{diag}(3/(3\lambda + 2\mu), 3/(2\mu), \mu^{-1}, \mu^{-1}, \mu^{-1})$ is the diagonal compliance matrix with the Lamé parameters λ and μ, $\underline{v} = [v_x \ v_y \ v_z]^T$ is the velocity vector and $\underline{\sigma} = [\omega \ \omega' \ \omega'' \ \sigma_{xy} \ \sigma_{xz} \ \sigma_{yz}]^T$ is the stress vector composed by linear combinations of the independent components of the stress tensor, proposed to factorize medium properties (Benjemaa et al., 2009). The first three components of the stress vector are $\omega = \frac{1}{3}(\sigma_{xx}+\sigma_{yy}+\sigma_{zz})$, $\omega' = \frac{1}{3}(2\sigma_{xx} - \sigma_{yy} - \sigma_{zz})$ and $\omega'' = \frac{1}{3}(-\sigma_{xx} + 2\sigma_{yy} - \sigma_{zz})$. The matrices $\underline{\underline{M}}_\theta$ and $\underline{\underline{N}}_\theta$ for all $\theta \in \{x, y, z\}$ are constant real matrices defined in Appendix A.

2.2 Fault boundary conditions and rate and state friction law

Rupture is described by the velocity field discontinuity over a known fault surface, Γ. The fault, Γ, is considered as an inner boundary where dynamic boundary conditions are imposed. It is convenient to arbitrarily identify a plus side (+), and a minus sign (−) of Γ to express the velocity, $\underline{v}$, over Γ as

$$\underline{v}^{\pm}(t, \underline{x}) = \lim_{\epsilon \to 0} \underline{v}(t, \underline{x} \pm \epsilon \underline{\hat{n}}(\underline{x})), \tag{3}$$

where $\epsilon \in \mathbb{R}$, $\underline{\hat{n}}(\underline{x})$ is the unit normal vector to the fault. For 3D simulations the fault, Γ, is simply a plane, or a set of adjacent planes. In the remainder of the manuscript, we omit the explicit dependence of the fields unless needed for clarity.

The velocity, $\underline{v}^{\pm}$, can be decomposed in its normal (N) and tangential (T) components

Artículo en prensa / Article in press

as

$$
\begin{aligned}
\underline{v}_N^{\pm} &= (\underline{\hat{n}} \cdot \underline{v}^{\pm})\underline{\hat{n}}, && (4) \\
\underline{v}_T^{\pm} &= \underline{v}^{\pm} - \underline{v}_N^{\pm} = \underline{v}^{\pm} - (\underline{\hat{n}} \cdot \underline{v}^{\pm})\underline{\hat{n}}. && (5)
\end{aligned}
$$

The discontinuity of the tangential velocity through Γ is known as the slip rate, $\underline{V}$, and is defined as

$$
\begin{aligned}
\underline{V}_T &:= [\![\underline{v}_T]\!] = \underline{v}_T^{+} - \underline{v}_T^{-}, && (6) \\
V &= \|\underline{V}_T\|, && (7)
\end{aligned}
$$

while the discontinuity of the normal component is

$$
\begin{aligned}
\underline{V}_N &:= [\![\underline{v}_N]\!] = \underline{v}_N^{+} - \underline{v}_N^{-}, && (8) \\
V_N &= \|\underline{V}_N\|, && (9)
\end{aligned}
$$

The frictional strength of the fault, τ, is determined with the Amontons-Coulomb model as

$$\tau = f(V,\psi)\sigma_N, \tag{10}$$

where $f(V,\psi)$ is the friction coefficient which is a function of the norm of the slip rate, V eq. (7), and the state variable, ψ, which can be interpreted as the average lifetime of the asperity population (Dieterich and Kilgore, 1996). This last variable allows modelling the fault healing after rupture, which is crucial for earthquake cycle simulations. When the normal component of the traction, $\underline{T}_N$, is compressive throughout the motion, then the normal stress over the fault can be computed as

$$\sigma_N = \|\underline{T}_N\|. \tag{11}$$

Tensile excursions can likewise be accommodated with only minor modifications (Day et al., 2005). With a rate and state friction law, the modulus of the tangential traction

Artículo en prensa / Article in press

is always equal to the shear strength of the fault, i.e. $\|\underline{T}_T\| = \tau$.

For the friction coefficient we use the regularized rate and state friction law

$$f(V,\psi) = a \cdot \operatorname{asinh}\left[\frac{V}{2V_0}\exp\left(\frac{\psi}{a}\right)\right], \tag{12}$$

where a is a frictional parameter and V_0 is the steady state sliding reference velocity. These types of friction law were first introduced by Dieterich (1979) and Ruina (1983) from small-scale laboratory experiments and have been widely used in numerical modeling of earthquake processes (Rice and Ben-Zion, 1996; Lapusta et al., 2000; Rice, 2001). The state variable evolves according to its own ordinary differential equation (ODE) as

$$d_t\psi = -\frac{V}{L}\left[\psi - \psi_{ss}(V)\right], \tag{13}$$

where L is a critical slip distance and $\psi_{ss}(V)$ is the state variable at steady state computed as

$$\psi_{ss}(V) = a \cdot \ln\left\{\frac{2V_0}{V}\sinh\left[\frac{f_{ss}(V)}{a}\right]\right\}, \tag{14}$$

where $f_{ss}(V)$ is the steady state friction

$$f_{ss}(V) = f_w + \frac{f_{LV}(V) - f_w}{\left[1 + (V/V_w)^8\right]^{1/8}}, \tag{15}$$

f_w and V_w are friction parameters and $f_{LV}(V)$ is the low-velocity steady state friction coefficient given by

$$f_{LV}(V) = f_0 - (b-a)\ln(V/V_0), \tag{16}$$

where b is another friction parameter. The rupture evolution strongly depends on the friction parameters a and b. Whenever $b > a$, the fault is velocity weakening; otherwise it is velocity strengthening. A velocity weakening region permits ruptures to nucleate and propagate, and therefore models a seismically strong-coupled surface (whereas rupture cannot nucleate in a velocity-strengthening region).

Artículo en prensa / Article in press

Finally, the last condition is

$$V\underline{T}_T = \tau \underline{V}, \tag{17}$$

which indicates that the slip rate must follow the same direction as the tangential traction.

3 Discrete equations with a discontinuous Galerkin method

To solve the hyperbolic system, eqs. (1) and (2), the domain Ω is discretized into a conforming mesh of K elements as

$$\Omega \simeq \Omega_h = \bigcup_{i=1}^{K} D^i, \tag{18}$$

where D^i is the i-th straight-sided tetrahedron of the mesh.

Following Etienne et al. (2010), a nodal Discontinuous Galerkin method with central fluxes and an explicit leap-frog time scheme is applied to eqs. (1) and (2) to obtain

$$\begin{aligned}
\rho^i \left(\underline{\underline{I}}_3 \otimes \underline{\underline{\mathcal{K}}}^i\right) \frac{\underline{v}^{\left(i,m+\frac{1}{2}\right)} - \underline{v}^{\left(i,m-\frac{1}{2}\right)}}{\Delta t} &= -\sum_{\theta \in \{x,y,z\}} \left(\underline{\underline{M}}_\theta \otimes \underline{\underline{\mathcal{E}}}^i_\theta\right) \underline{\sigma}^{(i,m)} \\
&\quad + \frac{1}{2} \sum_{k \in N^i} \left[\left(\underline{\underline{\mathcal{P}}}^{ik} \otimes \underline{\underline{\mathcal{F}}}^{ik}\right) \left(\underline{\sigma}^{(i,m)} + \underline{\sigma}^{(k,m)}\right)\right], & (19) \\
\left(\underline{\underline{\Lambda}}^i \otimes \underline{\underline{\mathcal{K}}}^i\right) \frac{\underline{\sigma}^{(i,m+1)} - \underline{\sigma}^{(i,m)}}{\Delta t} &= -\sum_{\theta \in \{x,y,z\}} \left(\underline{\underline{N}}_\theta \otimes \underline{\underline{\mathcal{E}}}^i_\theta\right) \underline{v}^{\left(i,m+\frac{1}{2}\right)} \\
&\quad + \frac{1}{2} \sum_{k \in N^i} \left[\left(\underline{\underline{\mathcal{Q}}}^{ik} \otimes \underline{\underline{\mathcal{F}}}^{ik}\right) \left(\underline{v}^{\left(i,m+\frac{1}{2}\right)} + \underline{v}^{\left(k,m+\frac{1}{2}\right)}\right)\right] & (20)
\end{aligned}$$

where m is the time index, N^i is the neighbor list of the i-tetrahedron, Δt is the time step size, $\underline{\underline{I}}_3$ is the identity matrix of $\mathbb{R}^3$, $\underline{\underline{\mathcal{K}}}^i$ is the mass matrix, $\underline{\underline{\mathcal{E}}}^i_\theta$ for $\theta \in \{x, y, z\}$ are the stiffness matrices, $\underline{\underline{\mathcal{F}}}^{ik}$ is the flux matrix and $\underline{\underline{\mathcal{P}}}^{ik}$ and $\underline{\underline{\mathcal{Q}}}^{ik}$ are defined in Appendix B. If we use second-order elements, we have a second order numerical scheme in space and time. We follow Tago et al. (2012) to separate the flux over the fault and to rewrite eqs.

Artículo en prensa / Article in press

(19) and (20) as

$$
\begin{aligned}
\underline{v}^{(i,m+\frac{1}{2})} &= \underline{v}^{(i,m-\frac{1}{2})} + \frac{\Delta t}{\rho^i}\left(\underline{\underline{I}}_3 \otimes \underline{\underline{\mathcal{K}}}^i\right)^{-1}\Bigg[-\sum_{\theta\in\{x,y,z\}}\left(\underline{\underline{M}}_\theta \otimes \underline{\underline{\mathcal{E}}}^i_\theta\right)\underline{\sigma}^{(i,m)} \\
&\quad + \frac{1}{2}\sum_{\substack{k\in N^i \\ D^i\cap D^k\not\subseteq\Gamma}}\left[\left(\underline{\underline{\mathcal{P}}}^{ik} \otimes \underline{\underline{\mathcal{F}}}^{ik}\right)\left(\underline{\sigma}^{(i,m)} + \underline{\sigma}^{(k,m)}\right)\right] \\
&\quad + \delta^\Gamma\left(\underline{\underline{I}}_3 \otimes \underline{\underline{\mathcal{F}}}^{ik}\right)\underline{\mathbb{F}}^{(\Gamma i,m+\frac{1}{2})}\Bigg], \qquad (21) \\
\underline{\sigma}^{(i,m+1)} &= \underline{\sigma}^{(i,m)} + \frac{\Delta t}{\rho^i}\left(\underline{\underline{\Lambda}}^i \otimes \underline{\underline{\mathcal{K}}}^i\right)^{-1}\Bigg[-\sum_{\theta\in\{x,y,z\}}\left(\underline{\underline{N}}_\theta \otimes \underline{\underline{\mathcal{E}}}^i_\theta\right)\underline{v}^{(i,m+\frac{1}{2})} \\
&\quad + \frac{1}{2}\sum_{\substack{k\in N^i \\ D^i\cap D^k\not\subseteq\Gamma}}\left[\left(\underline{\underline{\mathcal{Q}}}^{ik} \otimes \underline{\underline{\mathcal{F}}}^{ik}\right)\left(\underline{v}^{(i,n+\frac{1}{2})} + \underline{v}^{(k,n+\frac{1}{2})}\right)\right] \\
&\quad + \delta^\Gamma\left(\underline{\underline{I}}_3 \otimes \underline{\underline{\mathcal{F}}}^{ik}\right)\underline{\mathbb{G}}^{(\Gamma i,m+1)}\Bigg], \qquad (22)
\end{aligned}
$$

where δ^Γ is a Dirac delta function to identify fault faces and the fault fluxes, $\underline{\mathbb{F}}^{(\Gamma i,m+\frac{1}{2})}$ and $\underline{\mathbb{G}}^{(\Gamma i,m+1)}$ are defined as

$$
\begin{aligned}
\underline{\mathbb{F}}^{(\Gamma i,m+\frac{1}{2})} &= \underline{T}^{(\Gamma ik,m+\frac{1}{2})} = \underline{T}_N^{(\Gamma ik,m+\frac{1}{2})} + \underline{T}_T^{(\Gamma ik,m+\frac{1}{2})}, \qquad (23) \\
\underline{\mathbb{G}}^{(\Gamma i,m+1)} &= \underline{\underline{\mathcal{Q}}}^{ik}\underline{v}^{(i,m+\frac{1}{2})}, \qquad (24)
\end{aligned}
$$

and $\underline{T}_N^{(\Gamma ik,m+\frac{1}{2})}$ and $\underline{T}_T^{(\Gamma ik,m+\frac{1}{2})}$ are the normal and tangential tractions at the fault computed from the i-tetrahedron at time step m, respectively. The fault flux to update the stress vector, $\underline{\mathbb{G}}^{(\Gamma i,m+1)}$, only considers the velocity vector from the element in which that stress vector is computed.

If the integration of the Galerkin matrices, $\underline{\underline{\mathcal{K}}}^i$ and $\underline{\underline{\mathcal{F}}}^{ik}$, is done in the standard element (Zienkiewicz and Taylor, 2005), they can written as

$$
\underline{\underline{\mathcal{K}}}^i = \mathrm{W}^i\underline{\underline{\mathcal{K}}}^e, \quad \underline{\underline{\mathcal{F}}}^{ik} = S^{ik}\underline{\underline{\mathcal{F}}}^e, \qquad (25)
$$

where $\underline{\underline{\mathcal{K}}}^e$ is the standard mass matrix, $\underline{\underline{\mathcal{F}}}^{ik}$ is the standard flux matrix, W^i, is the volume of the i-tetrahedron and S^{ik} is the surface shared by the i- and k-tetrahedara.

Artículo en prensa / Article in press

Using the standard matrices, $\underline{\underline{\mathcal{K}}}^e$ and $\underline{\underline{\mathcal{F}}}^{ik}$, we can rewrite the update velocity scheme, eq. (21), as

$$\underline{v}^{(i,m+\frac{1}{2})} = \underline{v}^{(i,m-\frac{1}{2})} + \underline{R}^{(i,m)} + \frac{\delta^\Gamma \Delta t S^{ik}}{\rho^i W^i}\left(\underline{\underline{I}}_3 \otimes \underline{\underline{\mathcal{K}}}^{e^{-1}} \underline{\underline{\mathcal{F}}}^e\right)\left(\underline{T}_N^{\left(\Gamma ik,m+\frac{1}{2}\right)} + \underline{T}_T^{\left(\Gamma ik,m+\frac{1}{2}\right)}\right), \quad (26)$$

where

$$\begin{aligned}\underline{R}^{(i,m)} &= \frac{\Delta t}{\rho^i W^i}\left(\underline{\underline{I}}_3 \otimes \underline{\underline{\mathcal{K}}}^e\right)^{-1}\Bigg[-\sum_{\theta\in\{x,y,z\}}\left(\underline{\underline{M}}_\theta \otimes \underline{\underline{\mathcal{E}}}^i_\theta\right)\underline{\sigma}^{(i,m)} \\ &\quad + \frac{1}{2}\sum_{\substack{k\in N^i \\ D^i\cap D^k\not\subseteq\Gamma}}\left[\left(\underline{\underline{\mathcal{P}}}^{ik} \otimes \underline{\underline{\mathcal{F}}}^{ik}\right)\left(\underline{\sigma}^{(i,m)} + \underline{\sigma}^{(k,m)}\right)\right]\Bigg],\end{aligned} \quad (27)$$

contains the stiffness term and the non-fault fluxes.

The next subsections will explain how to compute the fault tractions, $\underline{T}_T^{\left(\Gamma ik,m+\frac{1}{2}\right)}$ and $\underline{T}_N^{\left(\Gamma ik,m+\frac{1}{2}\right)}$, that fulfill the rate and state friction law and the inner boundary conditions.

3.1 Fault tangential traction, $\underline{T}_T^{\left(\Gamma ik,m+\frac{1}{2}\right)}$, computation

Assuming that the i-tetrahedron is in the plus side of the fault, the slip rate between two adjacent tetrahedra can be computed from eq. (6) and the tangential projection of the velocity scheme, eq. (26), as

$$\begin{aligned}\underline{V}^{\left(i,m+\frac{1}{2}\right)} &= \underline{v}_T^{\left(i,m+\frac{1}{2}\right)} - \underline{v}_T^{\left(k,m+\frac{1}{2}\right)}, \\ &= \underline{V}^{\left(i,m-\frac{1}{2}\right)} + \underline{R}_T^{(i,m)} - \underline{R}_T^{(k,m)} + \frac{\delta^\Gamma \Delta t S^{ik}\left(\rho^i W^i + \rho^k W^k\right)}{\rho^i\rho^k W^i W^k}\left(\underline{\underline{I}}_3 \otimes \underline{\underline{\mathcal{K}}}^{e^{-1}} \underline{\underline{\mathcal{F}}}^e\right)\underline{T}_T^{\left(\Gamma ik,m+\frac{1}{2}\right)}\end{aligned} \quad (28)$$

The tangential fault traction, $\underline{T}_T^{\left(\Gamma ik,m+\frac{1}{2}\right)}$, can be decomposed in terms of the initial tangential traction, $\underline{T}_T^{(\Gamma ik,0)}$ and the total shear traction due to the friction evolution, $\underline{\mathcal{T}}_T^{\left(\Gamma ik,m+\frac{1}{2}\right)}$, as

$$\underline{T}_T^{\left(\Gamma ik,m+\frac{1}{2}\right)} = \underline{T}_T^{(\Gamma ik,0)} - \underline{\mathcal{T}}_T^{\left(\Gamma ik,m+\frac{1}{2}\right)}. \quad (29)$$

Artículo en prensa / Article in press

Then, the slip rate update in terms of the total shear traction can be written as

$$\underline{V}^{\left(i,m+\frac{1}{2}\right)} = \underline{\tilde{V}}^{\left(i,m+\frac{1}{2}\right)} - \left(\underline{\underline{I}}_3 \otimes \underline{\underline{C}}\right) \underline{\mathcal{T}}_T^{\left(\Gamma ik,m+\frac{1}{2}\right)}, \tag{30}$$

where

$$\underline{\underline{C}} = \frac{\delta^\Gamma \Delta t S^{ik}(\rho^i W^i + \rho^k W^k)}{\rho^i \rho^k W^i W^k} \underline{\underline{\mathcal{K}}}^{e^{-1}} \underline{\underline{\mathcal{F}}}^e, \tag{31}$$

and

$$\underline{\tilde{V}}^{\left(i,m+\frac{1}{2}\right)} = \underline{V}^{\left(i,m-\frac{1}{2}\right)} + \underline{R}_T^{(i,m)} - \underline{R}_T^{(k,m)} + \left(\underline{\underline{I}}_3 \otimes \underline{\underline{C}}\right) \underline{T}_T^{(\Gamma ik,0)}, \tag{32}$$

is the slip rate assuming a frictionless fault free surface, so it will be called *free slip rate*. Since the total tangential traction magnitude must equal the fault's shear strength, eq. (10), it should be computed as

$$\left\| \underline{\mathcal{T}}_T^{\left(\Gamma ik,m+\frac{1}{2}\right)} \right\| = \tau^{\left(\Gamma ik,m+\frac{1}{2}\right)} = f\left(V^{\left(i,m+\frac{1}{2}\right)}, \psi^{\left(i,m+\frac{1}{2}\right)}\right) \sigma_N^{(i,m)}. \tag{33}$$

Following a staggered time stepping of the velocity-state system, as done by Rojas et al. (2009), we decouple the state variable from the previous equation computing the friction coefficient with the state variable and the stresses simultaneously

$$\tau^{\left(\Gamma ik,m+\frac{1}{2}\right)} = f\left(V^{\left(i,m+\frac{1}{2}\right)}, \psi^{(i,m)}\right) \sigma_N^{(i,m)}. \tag{34}$$

So the state variable can be updated independently for each degree of freedom (DOF) located in the fault following the next steps:

1. Update the low-velocity steady state friction coefficient, eq. (16),

$$f_{LV}^{(i,m)}\left(V^{\left(i,m-\frac{1}{2}\right)}\right) = f_0^i - (b^i - a^i)\ln\left(V^{\left(i,m-\frac{1}{2}\right)}/V_0^i\right). \tag{35}$$

Artículo en prensa / Article in press

2. Compute the steady state friction coefficient, eq. (15),

$$f_{ss}^{(i,m)}\left(V^{\left(i,m-\frac{1}{2}\right)}\right) = f_w^i + \frac{f_{LV}^{(i,m)}\left(V^{\left(i,m-\frac{1}{2}\right)}\right) - f_w^i}{\left[1+\left(V^{\left(i,m-\frac{1}{2}\right)}/V_w^i\right)^8\right]^{1/8}}. \tag{36}$$

3. Update the steady state variable, eq. (14),

$$\psi_{ss}^{(i,m)}\left(V^{\left(i,m-\frac{1}{2}\right)}\right) = a^i \cdot \ln\left\{\frac{2V_0^i}{V^{\left(i,m-\frac{1}{2}\right)}}\sinh\left[\frac{f_{ss}^{(i,m)}\left(V^{\left(i,m-\frac{1}{2}\right)}\right)}{a^i}\right]\right\}. \tag{37}$$

4. Update the state variable with the exact solution of its ODE, eq. (13),

$$\begin{aligned}\psi^{(i,m)}\left(V^{\left(i,m-\frac{1}{2}\right)}\right) \quad &= \quad \psi^{(i,m-1)}\left(V^{\left(i,m-\frac{3}{2}\right)}\right)\exp\left(-\frac{V^{\left(i,m-\frac{1}{2}\right)}\Delta t}{L}\right) \\ &+\psi_{ss}^{(i,m)}\left(V^{\left(i,m-\frac{1}{2}\right)}\right)\left(1-\exp\left(-\frac{V^{\left(i,m-\frac{1}{2}\right)}\Delta t}{L}\right)\right).\end{aligned} \tag{38}$$

In order to compute the total tangential traction, $\underline{\mathcal{T}}_T^{\left(\Gamma ik,m+\frac{1}{2}\right)}$, the slip-rate norm , $V^{\left(i,m+\frac{1}{2}\right)}$, must be computed first. To do so, we must first recognize that the slip, as well as the free slip, should be parallel to the total tangential traction due to the slip direction condition, eq. (17), so we can write the slip rate update scheme, eq. (30), as

$$\underline{V}^{\left(i,m+\frac{1}{2}\right)} = (\underline{\underline{I}}_3 \otimes \underline{\underline{L}})\underline{\tilde{V}}^{\left(i,m+\frac{1}{2}\right)} - \left(\underline{\underline{I}}_3 \otimes \underline{\underline{CN}}\right)\underline{V}^{\left(i,m+\frac{1}{2}\right)}, \tag{39}$$

where $\underline{\underline{L}} = \mathrm{Diag}\left(\underline{\tilde{V}}_M^{\left(i,m+\frac{1}{2}\right)} \odot \underline{V}_M^{-1\left(i,m+\frac{1}{2}\right)}\right)$, $\underline{\underline{N}} = \mathrm{Diag}\left(\underline{\mathcal{T}}_{T_M}^{\left(\Gamma ik,m+\frac{1}{2}\right)} \odot \underline{V}_M^{-1\left(i,m+\frac{1}{2}\right)}\right)$, $\underline{\tilde{V}}_M^{\left(i,m+\frac{1}{2}\right)}$ is a vector with the norm of the free slip rate of all DOFs of the i-tetrahedron, $\underline{V}_M^{-1\left(i,m+\frac{1}{2}\right)}$ is a vector with the inverse of the norm of the slip rates of all DOFs of the i-tetrahedron, $\underline{\mathcal{T}}_{T_M}^{\left(\Gamma ik,m+\frac{1}{2}\right)}$ is a vector with the norm of the total tangential tractions of all DOFs of the i-tetrahedron and $\odot$ is the operator for the component-wise multiplication.

Substituting the total tangential traction with the Amontons-Coulomb model, eq. (10), and the friction coefficient, eq. (12), in eq. (39), it can be reformulated as a non-linear

Artículo en prensa / Article in press

equation, $\underline{r}(\cdot)$, that depends only on the magnitudes of the slip rates, $\underline{V}_M^{\left(i,m+\frac{1}{2}\right)}$, as

$$\underline{r}\left(\underline{V}_M^{\left(i,m+\frac{1}{2}\right)}\right) := \underline{V}_M^{\left(i,m+\frac{1}{2}\right)} + \underline{\underline{C}}\left(\underline{a}^i \cdot \operatorname{asinh}\left[\frac{\underline{V}_M^{\left(i,m+\frac{1}{2}\right)}}{2\underline{V}_0^i}\exp\left(\frac{\underline{\psi}^{(i,m)}}{\underline{a}^i}\right)\right]\underline{\sigma}_N^{(i,m)}\right) - \underline{\tilde{V}}_M^{\left(i,m+\frac{1}{2}\right)} = 0, \tag{40}$$

which is solved with a Newton-Raphson method to update the slip rate in every p-iteration as

$$\underline{V}_M^{\left(i,m+\frac{1}{2}\right)^{p+1}} = \underline{V}_M^{\left(i,m+\frac{1}{2}\right)^{p}} - \underline{\underline{J}}^{-1}\underline{r}\left(\underline{V}_M^{\left(i,m+\frac{1}{2}\right)^{p}}\right), \tag{41}$$

where $\underline{\underline{J}}$ is the Jacobian, which is defined in Appendix C.

Once the Newton-Raphson method has converged, the total tangential traction is computed as

$$\underline{\mathcal{T}}_T^{\left(\Gamma ik,m+\frac{1}{2}\right)} = \underline{f}\left(\underline{V}_M^{\left(i,m+\frac{1}{2}\right)}, \underline{\psi}^{(i,m)}\right) \odot \underline{\sigma}_N^{(i,m)} \odot \underline{\hat{\tilde{V}}}^{\left(i,m+\frac{1}{2}\right)}, \tag{42}$$

where $\underline{\hat{\tilde{V}}}^{\left(i,m+\frac{1}{2}\right)}$ is the normalized free slip.

Finally, to update the velocity in eq. (28), we evaluate the tangential traction, $\underline{T}_T^{\left(\Gamma ik,m+\frac{1}{2}\right)}$, using the total tangential traction, $\underline{\mathcal{T}}_T^{\left(\Gamma ik,m+\frac{1}{2}\right)}$, with eq. (42).

3.2 Fault normal traction, $\underline{T}_N^{\left(\Gamma ik,m+\frac{1}{2}\right)}$, computation

For the computation of the fault normal traction, $\underline{T}_N^{\left(\Gamma ik,m+\frac{1}{2}\right)}$, we force the continuity of the normal component of the velocity to avoid an opening mode during rupture, as

$$\underline{V}_N^{\left(i,m+\frac{1}{2}\right)} = \underline{v}_N^{\left(i,m+\frac{1}{2}\right)} - \underline{v}_N^{\left(k,m+\frac{1}{2}\right)} = 0. \tag{43}$$

We project the velocity update scheme, eq. (26), along the fault normal and substitute it in eq. (43) to clear the normal fault traction as

$$\underline{T}_N^{\left(\Gamma ik,m+\frac{1}{2}\right)} = \frac{\delta^\Gamma \rho^i \rho^k W^i W^k}{\Delta t S^{ik}(\rho^i W^i + \rho^k W^k)}\left(\underline{\underline{I}}_3 \times \underline{\underline{\mathcal{K}}}^e \underline{\underline{\mathcal{F}}}^{e^{-1}}\right)\left[-\underline{R}_N^{(i,m)} + \underline{R}_N^{(k,m)}\right]. \tag{44}$$

Artículo en prensa / Article in press

3.3 Artificial viscosity to attenuate numerical noise

The abrupt stress drop at the rupture front induces numerical noise in a high frequency band (HFO). This issue has been observed in diverse numerical methods, such as FDM (Day, 1982; Cruz-Atienza and Virieux, 2004; Day et al. 2005), FEM (Oglesby et al., 1998; Barall, 2009; Aagaard et al., 2013), FVM (Benjemaa et al., 2009) and DGM (Tago et al., 2012). Some DGM strategies have used upwind fluxes to solve the Riemann problem due to the velocity discontinuity along the fault, and because of their dissipative nature, they do not generate HFOs (De la Puente et al., 2009; Pelties et al., 2012; Zhang et al., 2023). However, the amount of dissipation and dispersion introduced depends strongly on the discretization and order of approximation. Instead of using an upwind flux, whose dissipative effect cannot be controlled, we opted for a simple, but very efficient, strategy used by Day (1982), and in subsequent papers, and described by Day et al. (2005), that introduces an artificial viscosity with a damped stress term for the motion equation, (1), as

$$\rho \partial_t \underline{v} = \sum_{\theta \in \{x,y,z\}} \partial_\theta \underline{\underline{M}}_\theta \left(\underline{\sigma} + \gamma \partial_t \underline{\sigma} \right), \tag{45}$$

where γ is an artificial damping parameter.

Rojas et al. (2009) made a detailed analysis of this damping parameter, γ, and showed that for a given discretization and small values of γ, the absorption-wavelength spectrum can be far separated from the cohesive zone dimension. This means that the physical wavelength spectrum is practically unaffected and only the HFOs are eliminated. This strategy is appealing for energy conservative numerical schemes like ours (due to the central fluxes and the ad hoc fault fluxes). The damping parameter, γ, will be discussed in the following section.

The DGM implementation of the artificial damping is straightforward; instead of using $\underline{\sigma}^{(i,m)}$ in the velocity update scheme, eq. (21), we use the damped stresses, $\underline{\sigma}^{(i,m)}_{\text{damped}} = \underline{\sigma}^{(i,m)} + \gamma \frac{\sigma^{(i,m)} - \sigma^{(i,m-1)}}{\Delta t}$.

Artículo en prensa / Article in press

4 Results

The verification and performance assessment of our numerical implementation was done by solving the benchmark TPV104 from SCEC (Harris et al., 2018).

4.1 TPV104 SCEC benchmark

The TPV104 is a strike-slip planar fault embedded in an isotropic, homogeneous linearly elastic half-space that reaches the free surface. The hypocenter is located in the middle of a velocity-weakening portion of dimensions of 30 km $\times$ 15 km. At its borders, there is a 3 km zone of transition from velocity-weakening to velocity-strengthening, beyond which the fault is velocity-strengthening. The values of all the friction-law parameters, initial conditions and the nucleation parameters can be found in the benchmark website `https://strike.scec.org/cvws/tpv103_104docs.html`. The locations of the nine on-fault stations and six free-surface stations can also be consulted.

We use Gmsh software (Geuzaine and Remacle, 2009) to discretize the domain with a tetrahedral conforming mesh. The fault plane is defined before the mesh generation, such that it cannot be crossed by any tetrahedron. For subsections 4.2 and 4.3, we discretized the fault with an edge-length characteristic size of 100 m. Since we use second-order elements, the distance between DOFs along the edge length is 50 m.

We start by evaluating the effect of the artificial damping parameter, γ, on dispersion and accuracy of our solution. Then, due to the absence of an analytical solution, we compare our results with those obtained using other numerical strategies. Finally, we evaluate the convergence as a function of grid refinement.

4.2 Artificial damping

As clearly stated by Rojas et al. (2009), the larger the value of γ, the smaller the amplitude of the HFOs. However, large γ can also lead to overdamped solutions and a significant delay in the rupture front.

Fig. 1 shows the shear stress and slip rate using the damping factors $\gamma = \{0.0, 0.1, 0.2, 0.3, 0.4\}$,

Artículo en prensa / Article in press

registered on one of the farthest on-fault stations located 12 km along strike and 12 km along dip from the hypocenter. From Figs. 1.a and 1.d, we do not observe a significant difference for those γ values in the shear stress and slip rate, respectively. To better appreciate the difference in the the shear stress, we made zooms around the peak shear stress, Fig. 1.b, and the noisiest time interval, Fig. 1.c, respectively. The maximum per cent difference of the peak shear stress with respect the non-damping solution, $\gamma = 0.0$, was of 0.0709% for $\gamma = 0.4$. And also for $\gamma = 0.4$, the maximum percent difference in the delay between peak shear stresses, relative to the undamped solution, is 0.2672%. When assessing the noisest time interval, we find a strong reduction of the HFOs. Since for $\gamma = 0.1$ we still observe small high frequency oscillations, we choose $\gamma = 0.2$ as an optimal value. For the slip rate, the HFOs were eliminated for all $\gamma > 0$ (see Fig. 1.f). As illustrated in Fig. 1.e, the peak slip rate differences are almost negligible; the maximum percent difference relative to the undamped solution was 1.1141% for $\gamma = 0.4$ and for $\gamma = 0.2$ it was 0.4093%. It is important to state that optimal γ is $h-$dependent, however Rojas et al. (2009) showed that for $\gamma \in (0, 0.1]$ the HFOs are satisfactorily removed without perturbing the important features of the undamped solution.

Fig. 2 shows the convergence results with common selected rupture features to assess the accuracy (Day et al., 2005; Pelties et al., 2012; Zhang et al., 2023). The damped solutions for $\gamma = \{0.1, 0.2, 0.3, 0.4\}$ are compared with the undamped solution, $\gamma = 0.0$, by computing the Root Mean Squared Percentage Error (RMSPE) of the rupture time along the fault (Fig. 2.a), the RMSPE peak slip rate (Fig. 2.b) and the RMSPE final slip (Fig. 2.c), with the latter two considering all the on-fault stations of the benchmark. The convergence rates are 0.4952 for the rupture time, 1.0382 for the peak slip rate, and 0.7324 for the final slip. All convergence rates in the range of $\gamma = [0.1, 0.4]$ are small as expected from the previous analysis of Fig. 1. So even with large values of γ, compared to the recommendation of $\gamma < 0.1$, we still preserve the main features of the rupture propagation. The peak slip rate is the most sensitive to the damping parameter, so it would be an adequate feature to compare with other numerical solutions. Our solutions in the next subsection were computed with our selected optimal damping factor $\gamma = 0.2$,

Artículo en prensa / Article in press

whose RMSPE values for rupture time, peak slip rate, and final slip are 0.3528, 1.0040, and 0.1861, respectively.

4.3 Waveform assessment

Since no analytical solutions exist for dynamic rupture problems, we selected three numerical approaches for comparison with our solution. These reference solutions were computed with a roughly comparable DOF density in order to illustrate the variability among similar methods. One exception was deliberately oversampled by a factor of four to serve as a high-precision benchmark. It is important to note that equalizing the DOF density should not be interpreted as a basis for ranking the methods, as DOF density is not directly related to computational cost.

The numerical schemes selected for comparison were FaultMod, a FEM code (Barall, 2009); SPECFEM3D, a SEM code (Ampuero, 2002; Kaneko et al., 2008); and MixF-DG, a DGM code (Zhang et al., 2023). FaultMod is a first-order FEM code that employs Newmark time integration, artificial damping to mitigate HFOs and a grid-doubling technique for mesh refinement near the fault. An element size of 50 m was used for TPV104, corresponding to the recommended spacing between DOFs for this benchmark. This strategy has been used as a reference for all SCEC benchmarks since it was developed by the same group in charge of SCEC benchmarks development. SPECFEM3D is SEM with an adapted Newark time integration and without artificial damping. The fault element size was also 50 m with 5 Gauss-Lobato-Legendre (GLL) nodes per edge for fourth order elements. The distribution of the GLL nodes is not equidistant, but we consider a DOF's equivalent distance of 12.5 m. Finally, MixF-DG is the most recent DGM reported to date with upwind fluxes everywhere except on the off-fault fluxes of the on-fault elements where central fluxes are implemented. It does not add artificial damping due to the upwind on fault flux that does not generate HFOs. The use of central fluxes prevents spatial spike oscillations (SSO) generated by large on-fault stress drops and the use of upwind fluxes. These SSOs are strongly mesh-dependent and can lead to instabilities, specially with near-fault mesh refinement. The fault element size was 200 m with fourth order

Artículo en prensa / Article in press

elements as well. The node distribution is optimal and not equidistant (Hesthaven and Warburton, 2007), but we consider the DOFs equivalent distance of 50 m. For DGCrack we use second order elements with a fault element size of 100 m, i.e. a 50 m DOFs equivalent distance. Since, of all strategies, SPECFEM3D has the smallest DOFs distance and it does not add any damping procedure, explicitly nor implicitly, it was selected as our reference solution. FaultMod and SPECFEM3D discretize the medium using hexahedral elements, whereas MixF-DG and DGCrack use tetrahedral elements.

In Fig. 3, the rupture velocity along the fault is in good agreement among all solutions except for FaultMod solution, where a rupture delay can clearly be observed at the edges. On-fault records of the shear stress and the slip rate are shown in Fig. 4. On-fault records located 9 km along strike and 7.5 km along dip from the hypocenter are shown in Figs. 4.a and 4.b. Those located 12 km along strike and 3 km along dip from the hypocenter are shown in Figs. 4.e and 4.g. All of them are quite similar, with a small delay of the FaultMod solution, as was expected from the rupture time contour plots (Fig. 3). This delay can be better appreciated in the zoom insets around the peaks of the shear stress and the slip rate, Figs. 4.f and 4.h, respectively. The SPECFEM3D solution is the only one that we expect to have no delay since it has the smallest DOF spacing and no damping was applied. Afterwards, the order of the rupture front is DGCrack, MixF-DG and FaultMod, which can be appreciated in the peak shear stress delay in Fig. 4.f. Thus, with our (explicitly imposed) artificial damping, the dispersion is smaller than that produced by the implicit damping of the upwind flux from MixF-DG. However, artificial damping requires the specification of a hyperparameter, γ, which must be tuned through numerical tests or heuristic rules. Comparing the peak slip rate at a single station is challenging, as the differences may be more related to interpolation effects than to attenuation artifacts. Fig. 4.h shows that MixF-DG has the lowest amplitude, but it would be better to assess the differences considering all fault stations (Fig. 6.b).

The noise in the on-fault records seems negligible for all numerical approaches (see Fig. 4.c). However, this is not the case for the the off-fault records. Fig. 5 shows the velocity field registered at a free surface station located 12 km along strike and 6 km perpendicu-

Artículo en prensa / Article in press

lar to the fault. It should be noticed that not all noise comes from the strong singularity evolution of the rupture front, but it can also be due to the mesh coarsening used by the different strategies for better computational performance. Unfortunately, the noise differentiation for the different strategies is not possible, so we will assume that most of the noise comes from the dynamic rupture modeling. All numerical approches show noise in the records but with different frequency content. As it is expected, SPECFEM3D has the largest peak velocities (Figs. 5.b, 5.d and 5.f) but also the largest HFOs. In amplitude, our solution, DGCrack, seems to be closest to SPECFEM3D. FaultMod and MixF-DG seems to have similar peak velocities with even smaller values. It should be noticed that MixF-DG shows the cleanest records and the same phase arrivals as the rest of the solutions.

Fig. 6 shows the RMSPE for the on-fault metrics used by Zhang et al. (2023), which includes the rupture time along the fault and the peak slip rate and the final slip recorded at nine on-fault stations. The RMSPEs are computed using the SPECFEM3D solution as the reference, due to its finer fault discretization. We can observe that for all these metrics DGCrack is closest to SPECFEM3D, followed closely by MixF-DG. In every metric, DGCrack achieves a RMSPE roughly 50% lower than MixF-DG's. FaultMod shows the worst RMPSEs, but as shown in Fig. 4, the on-fault records are almost noise-free and similar to the other solutions.

We have shown that DGCrack's solution is in agreement with other numerical strategies. In the next section we will show its convergence under grid refinement.

4.4 Convergence under grid refinement

In this section, we assess the accuracy according to the grid size. We solved TPV104 for different element sizes, $h = \{100, 150, 200, 300, 400\}\ m$, with the previously selected artificial damping parameter $\gamma = 0.2$.

Fig. 7 shows that the horizontal shear stress and the slip rate for the different discretizations are quite similar even with the discretization of $h = 300\ m$ that is three times larger than the suggested discretization for the cohesive zone. Fig. 7.c shows low frequency

Artículo en prensa / Article in press

noise that seems to get stronger with grid coarsening. A slight delay in the rupture front is more clearly visible in the zoomed views around the peak shear stress and slip rate (Figs. 7.f and 7.h, respectively). However, it is remarkable how the peak slip rate remains nearly identical across all discretizations.

The convergence rates are shown in Fig. 8 as a function of grid refinement. The convergence rates for the rupture time, the peak slip rate and the final slip, were 1.6008, 0.6774 and 1.4470, respectively. These low convergence rates are expected due to the nonlinearity of the friction equations. Moreover, higher-order approximations do not improve the convergence rates, as has been shown numerically (Zhang et al., 2023; Pelties et al., 2012).

5 Discussion and Conclusions

We have implemented a rate-and-state friction law in DGCrack (Tago et al., 2012), inspired by the work of Rojas et al. (2009). The friction coefficient computation is done with a staggered time strategy for the velocity-state system. Unlike previous implementations with DGM (e.g. Pelties et al., 2012; Zhang et al., 2023), we do not employ an upwind flux; instead, we use an ad hoc flux along the fault. While an upwind flux naturally suppresses HFOs due to its intrinsic dissipation, the magnitude of the dissipation and dispersion introduced has not been studied in detail.

Our ad hoc fault flux generates HFOs, which we attenuated using an artificial damping strategy. This required the introduction of a damping parameter that needs tuning. As previously shown by Rojas et al. (2009), for $\gamma < 0.1$ the damped frequency band lies above the frequency band in which the undamped numerical scheme has effectively converged, so almost no unwanted damping is applied. In practice, the phase delay produced by the artificial damping is more noticeable than any amplitude reduction. However, as illustrated in Figs. 4 and 2, these effects are negligible. For the TPV104 case, we chose a larger damping parameter than the recommended value, $\gamma = 0.2$, to eliminate all visible noise. For earthquake simulations, however, we recommend starting with a conservative

Artículo en prensa / Article in press

value of $\gamma = 0.1$, increasing it only if HFOs persist.

In the waveform comparison, DGCrack demonstrated good performance relative to recent and validated numerical strategies. For the fault metrics shown in Fig. 6, our solution was closer to the reference than that of MixF-DG, even though MixF-DG employed a higher-order approximation. Furthermore, dissipation and dispersion in DGCrack fault fields were smaller than in MixF-DG fault fields (see Figs. 4.f and 4.h). These numerical artifacts appear to arise more from the upwind flux used in MixF-DG than from the artificial damping introduced in our approach.

Convergence rates from grid refinement are inherently limited by the nonlinearity of dynamic rupture modeling. For DGCrack, the convergence rates obtained are relatively low, as expected from the earlier numerical comparison of the SCEC slip-weakening TPV3 benchmark by Zhang et al. (2023). This should not be viewed as a drawback, since our solution delivers accuracy comparable to higher-order approximations. Moreover, for coarser grids DGCrack should outperform high-order numerical strategies due to its relatively low convergence rates (see Fig. 7.h).

Although we have shown that for $\gamma < 0.1$ the fault field spectra are largely preserved, the need to introduce a damping parameter may be seen as a disadvantage compared with approaches that use upwind fluxes to avoid HFOs. However, since numerical damping is necessary, it may be better to have a control parameter for it, rather than it being implicit in a numerical flux. We believe that an upwind flux formulation with controlled dissipation and dispersion still needs to be developed to address this limitation.

Finally, we plan to apply DGCrack to simulate earthquakes in Mexico, using friction parameters and initial conditions inferred from seismotectonic studies (Cruz-Atienza et al., 2021).

Artículo en prensa / Article in press

Author Contributions: Conceptualization, J.T.; methodology, J.T. and S.M.D.; software, J.T.; validation, J.T. and S.M.D.; formal analysis, J.T., S.M.D., V.M.C.-A. and C.V.; resources, S.M.D.; writing—original draft preparation, J.T.; writing—review and editing, J.T., S.M.D., V.M.C.-A. and C.V.; funding acquisition, J.T.. All authors have read and agreed to the published version of the manuscript.

Funding: This research was supported by JST SATREPS Japan Grant Number JPMJSA2310 and by UNAM-PAPIIT grant IN109225.

Acknowledgments: The authors thank the Editor, Dr. Carlos Mendoza, and the reviewers, Dr. Alejandro Gaytan and Dr. Carlos Huerta, for their constructive comments and valuable suggestions, which helped improve the manuscript.

Data Availability Statement: The numerical solutions used for the comparison can be downloaded at `https://strike.scec.org/cvws/cgi-bin/cvws.cgi`. The DGCrack solution is available from the authors upon request

.

Conflicts of Interest: The authors declare no conflicts of interest.

Artículo en prensa / Article in press

Appendices

A Matrices of the first-order elastodynamic equations

The matrices $\underline{\underline{M}}_\theta$ and $\underline{\underline{N}}_\theta$ for all $\theta \in \{x, y, z\}$ are

$$
\underline{\underline{M}}_x = \begin{pmatrix} 1 & 1 & 0 & 0 & 0 & 0 \\ 0 & 0 & 0 & 1 & 0 & 0 \\ 0 & 0 & 0 & 0 & 1 & 0 \end{pmatrix}, \quad \underline{\underline{N}}_x = \begin{pmatrix} 1 & 2 & -1 & 0 & 0 & 0 \\ 0 & 0 & 0 & 1 & 0 & 0 \\ 0 & 0 & 0 & 0 & 1 & 0 \end{pmatrix}^T,
$$

$$
\underline{\underline{M}}_y = \begin{pmatrix} 0 & 0 & 0 & 1 & 0 & 0 \\ 1 & 0 & 1 & 0 & 0 & 0 \\ 0 & 0 & 0 & 0 & 0 & 1 \end{pmatrix}, \quad \underline{\underline{N}}_y = \begin{pmatrix} 0 & 0 & 0 & 1 & 0 & 0 \\ 1 & -1 & 2 & 0 & 0 & 0 \\ 0 & 0 & 0 & 0 & 0 & 1 \end{pmatrix}^T
$$

$$
\underline{\underline{M}}_z = \begin{pmatrix} 0 & 0 & 0 & 0 & 1 & 0 \\ 0 & 0 & 0 & 0 & 0 & 1 \\ 1 & -1 & -1 & 0 & 0 & 0 \end{pmatrix}, \quad \underline{\underline{N}}_z = \begin{pmatrix} 0 & 0 & 0 & 0 & 1 & 0 \\ 0 & 0 & 0 & 0 & 0 & 1 \\ 1 & -1 & -1 & 0 & 0 & 0 \end{pmatrix}^T.
$$

Artículo en prensa / Article in press

B Matrices of the discontinuous Galerkin discretization

The fluxes matrices of the DGM discretization of eqs. (19) and (20) are

$$
\begin{aligned}
\underline{\underline{\mathcal{P}}}^{ik} &= \sum_{\theta\in\{x,y,z\}} \hat{n}_\theta^{ik} \underline{\underline{M}}_\theta, \\
&= \begin{bmatrix} \hat{n}_x^{ik} & \hat{n}_x^{ik} & 0 & \hat{n}_y^{ik} & \hat{n}_z^{ik} & 0 \\ \hat{n}_y^{ik} & 0 & \hat{n}_y^{ik} & \hat{n}_x^{ik} & 0 & \hat{n}_z^{ik} \\ \hat{n}_z^{ik} & -\hat{n}_z^{ik} & -\hat{n}_z^{ik} & 0 & \hat{n}_x^{ik} & \hat{n}_y^{ik} \end{bmatrix}, \\
\underline{\underline{\mathcal{Q}}}^{ik} &= \sum_{\theta\in\{x,y,z\}} \hat{n}_\theta^{ik} \underline{\underline{N}}_\theta, \\
&= \begin{bmatrix} \hat{n}_x^{ik} & 2\hat{n}_x^{ik} & -\hat{n}_x^{ik} & \hat{n}_y^{ik} & \hat{n}_z^{ik} & 0 \\ \hat{n}_y^{ik} & -\hat{n}_y^{ik} & 2\hat{n}_y^{ik} & \hat{n}_x^{ik} & 0 & \hat{n}_z^{ik} \\ \hat{n}_z^{ik} & -\hat{n}_z^{ik} & -\hat{n}_z^{ik} & 0 & \hat{n}_x^{ik} & \hat{n}_y^{ik} \end{bmatrix}^T.
\end{aligned}
$$

C Jacobian

The Jacobian of eq. (40) is

$$
J_{kl}\left(V_M^{\left(i,m+\frac{1}{2}\right)}\right) = \left[\frac{\partial r_k}{\partial V_{M_l}^{\left(i,m+\frac{1}{2}\right)}}\right],
$$

where

$$
\begin{aligned}
J_{kk} &= 1 + \frac{C_{kk} a_k^i \sigma_{N_k}^{(i,m)} \exp\left(\frac{\psi_k^{(i,m)}}{a_k^i}\right)}{2V_{0_k}^i \sqrt{1 + \left(\frac{V_{M_k}^{\left(i,m+\frac{1}{2}\right)}}{2V_{0_k}^i} \exp\left(\frac{\psi_k^{(i,m)}}{a_k^i}\right)\right)^2}}, \\
J_{kl} &= \frac{C_{kl} a_l^i \sigma_{N_l}^{(i,m)} \exp\left(\frac{\psi_l^{(i,m)}}{a_l^i}\right)}{2V_{0_l}^i \sqrt{1 + \left(\frac{V_{M_l}^{\left(i,m+\frac{1}{2}\right)}}{2V_{0_l}^i} \exp\left(\frac{\psi_l^{(i,m)}}{a_l^i}\right)\right)^2}}.
\end{aligned}
$$

Artículo en prensa / Article in press

References

Aagaard, B. T., Knepley, M. G., and Williams, C. A. (2013). A domain decomposition approach to implementing fault slip in finite-element models of quasi-static and dynamic crustal deformation. Journal of Geophysical Research: Solid Earth, 118(6):3059–3079.

Ampuero, J.-P. (2002). Etude physique et numérique de la nucléation des séismes. PhD thesis, Paris 7.

Ando, R. and Kaneko, Y. (2018). Dynamic rupture simulation reproduces spontaneous multifault rupture and arrest during the 2016 mw 7.9 kaikoura earthquake. Geophysical Research Letters, 45(23):12–875.

Andrews, D. (1985). Dynamic plane-strain shear rupture with a slip-weakening friction law calculated by a boundary integral method. Bulletin of the Seismological Society of America, 75(1):1–21.

Andrews, D. J. (1976). Rupture propagation with finite stress in antiplane strain. Journal of Geophysical Research (1896-1977), 81(20):3575–3582.

Aochi, H. and Cruz-Atienza, V. M. (2025). Rupture dynamics and near-fault ground motion of the mw7. 8 kahramanmaraş, turkey earthquake of february 6, 2023. Seismica, 4:1432.

Barall, M. (2009). A grid-doubling finite-element technique for calculating dynamic three-dimensional spontaneous rupture on an earthquake fault. Geophysical Journal International, 178(2):845–859.

Benjemaa, M., Glinsky-Olivier, N., Cruz-Atienza, V., Virieux, J., and Piperno, S. (2007). Dynamic non-planar crack rupture by a finite volume method. Geophysical Journal International, 171(1):271–285.

Benjemaa, M., Glinsky-Olivier, N., Cruz-Atienza, V. M., and Virieux, J. (2009). 3-d dynamic rupture simulations by a finite volume method. Geophysical Journal International, 178(1):541–560.

Artículo en prensa / Article in press

Cruz-Atienza, V. and Virieux, J. (2004). Dynamic rupture simulation of non-planar faults with a finite-difference approach. Geophysical Journal International, 158(3):939–954.

Cruz-Atienza, V. M., Tago, J., Villafuerte, C., Wei, M., Garza-Girón, R., Dominguez, L. A., Kostoglodov, V., Nishimura, T., Franco, S., Real, J., et al. (2021). Short-term interaction between silent and devastating earthquakes in mexico. Nature communications, 12(1):2171.

Dalguer, L. A. and Day, S. M. (2007). Staggered-grid split-node method for spontaneous rupture simulation. Journal of Geophysical Research: Solid Earth, 112(B2).

Das, S. and Aki, K. (1977). A numerical study of two-dimensional spontaneous rupture propagation. Geophysical journal international, 50(3):643–668.

Day, S. M. (1982). Three-dimensional simulation of spontaneous rupture: the effect of nonuniform prestress. Bulletin of the Seismological Society of America, 72(6A):1881–1902.

Day, S. M., Dalguer, L. A., Lapusta, N., and Liu, Y. (2005). Comparison of finite difference and boundary integral solutions to three-dimensional spontaneous rupture. Journal of Geophysical Research: Solid Earth, 110(B12).

Day, S. M. and Ely, G. P. (2002). Effect of a shallow weak zone on fault rupture: Numerical simulation of scale-model experiments. Bulletin of the Seismological Society of America, 92(8):3022–3041.

De la Puente, J., Ampuero, J.-P., and Käser, M. (2009). Dynamic rupture modeling on unstructured meshes using a discontinuous galerkin method. Journal of Geophysical Research: Solid Earth, 114(B10).

Dieterich, J. H. (1979). Modeling of rock friction: 1. experimental results and constitutive equations. Journal of Geophysical Research: Solid Earth, 84(B5):2161–2168.

Dieterich, J. H. and Kilgore, B. (1996). Implications of fault constitutive properties for

Artículo en prensa / Article in press

earthquake prediction. Proceedings of the National Academy of Sciences, 93(9):3787–3794.

Erickson, B. A., Jiang, J., Barall, M., Lapusta, N., Dunham, E. M., Harris, R., Abrahams, L. S., Allison, K. L., Ampuero, J.-P., Barbot, S., et al. (2020). The community code verification exercise for simulating sequences of earthquakes and aseismic slip (seas). Seismological Research Letters, 91(2A):874–890.

Erickson, B. A., Jiang, J., Lambert, V., Barbot, S. D., Abdelmeguid, M., Almquist, M., Ampuero, J.-P., Ando, R., Cattania, C., Chen, A., et al. (2023). Incorporating full elastodynamic effects and dipping fault geometries in community code verification exercises for simulations of earthquake sequences and aseismic slip (seas). Bulletin of the Seismological Society of America, 113(2):499–523.

Etienne, V., Chaljub, E., Virieux, J., and Glinsky, N. (2010). An hp-adaptive discontinuous galerkin finite-element method for 3-d elastic wave modelling. Geophysical Journal International, 183(2):941–962.

Galis, M., Moczo, P., Kristek, J., and Kristekova, M. (2010). An adaptive smoothing algorithm in the tsn modelling of rupture propagation with the linear slip-weakening friction law. Geophysical Journal International, 180(1):418–432.

Galvez, P., Ampuero, J.-P., Dalguer, L. A., Somala, S. N., and Nissen-Meyer, T. (2014). Dynamic earthquake rupture modelled with an unstructured 3-d spectral element method applied to the 2011 m 9 tohoku earthquake. Geophysical Journal International, 198(2):1222–1240.

Geuzaine, C. and Remacle, J.-F. (2009). Gmsh: A 3-d finite element mesh generator with built-in pre-and post-processing facilities. International journal for numerical methods in engineering, 79(11):1309–1331.

Harris, R. A., Barall, M., Aagaard, B., Ma, S., Roten, D., Olsen, K., Duan, B., Liu, D., Luo, B., Bai, K., et al. (2018). A suite of exercises for verifying dynamic earthquake rupture codes. Seismological Research Letters, 89(3):1146–1162.

Artículo en prensa / Article in press

Hesthaven, J. S. and Warburton, T. (2007). Nodal discontinuous Galerkin methods: algorithms, analysis, and applications. Springer Science & Business Media.

Kaneko, Y., Lapusta, N., and Ampuero, J.-P. (2008). Spectral element modeling of spontaneous earthquake rupture on rate and state faults: Effect of velocity-strengthening friction at shallow depths. Journal of Geophysical Research: Solid Earth, 113(B9).

Käser, M. and Dumbser, M. (2006). An arbitrary high-order discontinuous galerkin method for elastic waves on unstructured meshesi. the two-dimensional isotropic case with external source terms. Geophysical Journal International, 166(2):855–877.

Kozdon, J. E., Dunham, E. M., and Nordström, J. (2012). Interaction of waves with frictional interfaces using summation-by-parts difference operators: Weak enforcement of nonlinear boundary conditions. Journal of Scientific Computing, 50:341–367.

Kozdon, J. E., Dunham, E. M., and Nordström, J. (2013). Simulation of dynamic earthquake ruptures in complex geometries using high-order finite difference methods. Journal of Scientific Computing, 55:92–124.

Lapusta, N., Rice, J. R., Ben-Zion, Y., and Zheng, G. (2000). Elastodynamic analysis for slow tectonic loading with spontaneous rupture episodes on faults with rate-and state-dependent friction. Journal of Geophysical Research: Solid Earth, 105(B10):23765–23789.

LeVeque, R. J. (2002). Finite volume methods for hyperbolic problems, volume 31. Cambridge university press.

Madariaga, R., Olsen, K., and Archuleta, R. (1998). Modeling dynamic rupture in a 3d earthquake fault model. Bulletin of the Seismological Society of America, 88(5):1182–1197.

Moczo, P., Kristek, J., Galis, M., Pazak, P., and Balazovjech, M. (2007). The finite-difference and finite-element modeling of seismic wave propagation and earthquake motion. Acta physica slovaca, 57(2).

Artículo en prensa / Article in press

Oglesby, D. D., Archuleta, R. J., and Nielsen, S. B. (1998). Earthquakes on dipping faults: The effects of broken symmetry. Science, 280(5366):1055–1059.

Oglesby, D. D., Archuleta, R. J., and Nielsen, S. B. (2000). Dynamics of dip-slip faulting: Explorations in two dimensions. Journal of Geophysical Research: Solid Earth, 105(B6):13643–13653.

Pelties, C., De la Puente, J., Ampuero, J.-P., Brietzke, G. B., and Käser, M. (2012). Three-dimensional dynamic rupture simulation with a high-order discontinuous galerkin method on unstructured tetrahedral meshes. Journal of Geophysical Research: Solid Earth, 117(B2).

Pelties, C., Gabriel, A.-A., and Ampuero, J.-P. (2014). Verification of an ader-dg method for complex dynamic rupture problems. Geoscientific Model Development, 7(3):847–866.

Qian, F., Wu, B., Feng, X., and Zhang, H. (2019). 3d numerical simulation of dynamic ruptures on complex fault systems by biem with unstructured meshes. Chinese Journal of Geophysics, 62(9):3421–3431.

Rice, J. R. (2001). New perspectives on crack and fault dynamics. In Mechanics for a New Mellennium: Proceedings of the 20th International Congress of Theoretical and Applied Mechanics Chicago, Illinois, USA 27 August–2 September 2000, pages 1–24. Springer.

Rice, J. R. and Ben-Zion, Y. (1996). Slip complexity in earthquake fault models. Proceedings of the National Academy of Sciences, 93(9):3811–3818.

Rojas, O., Day, S., Castillo, J., and Dalguer, L. A. (2008). Modelling of rupture propagation using high-order mimetic finite differences. Geophysical Journal International, 172(2):631–650.

Rojas, O., Dunham, E. M., Day, S. M., Dalguer, L. A., and Castillo, J. E. (2009). Finite difference modelling of rupture propagation with strong velocity-weakening friction. Geophysical Journal International, 179(3):1831–1858.

Artículo en prensa / Article in press

Ruina, A. (1983). Slip instability and state variable friction laws. Journal of Geophysical Research: Solid Earth, 88(B12):10359–10370.

Tago, J., Cruz-Atienza, V. M., Virieux, J., Etienne, V., and Sánchez-Sesma, F. J. (2012). A 3d hp-adaptive discontinuous galerkin method for modeling earthquake dynamics. Journal of Geophysical Research: Solid Earth, 117(B9).

Zhang, W., Liu, Y., and Chen, X. (2023). A mixed-flux-based nodal discontinuous galerkin method for 3d dynamic rupture modeling. Journal of Geophysical Research: Solid Earth, 128(6):e2022JB025817.

Zienkiewicz, O. C. and Taylor, R. L. (2005). The finite element method for solid and structural mechanics. Elsevier.

Artículo en prensa / Article in press

Figures

Artículo en prensa / Article in press

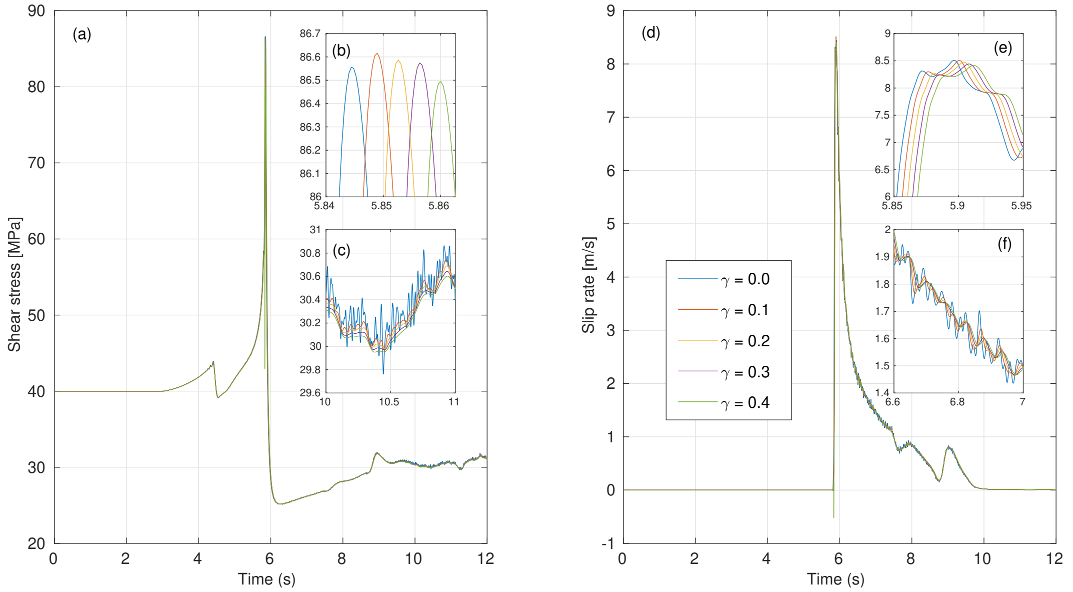

Figure 1: On-fault records for damping factors, $\gamma = \{0.0, 0.1, 0.2, 0.3, 0.4\}$, of the shear stress $[MPa]$, (a), and slip rate $[m/s]$, (d), at the fault station located 12 km along strike and 12 km along dip from the hypocenter. (b) and (c) are zoom figures of the peak slip rate and the noisest slip rate time interval, respectively. (e) and (f) are zoom figures of the peak shear stress and the noisest shear stress time interval, respectively.

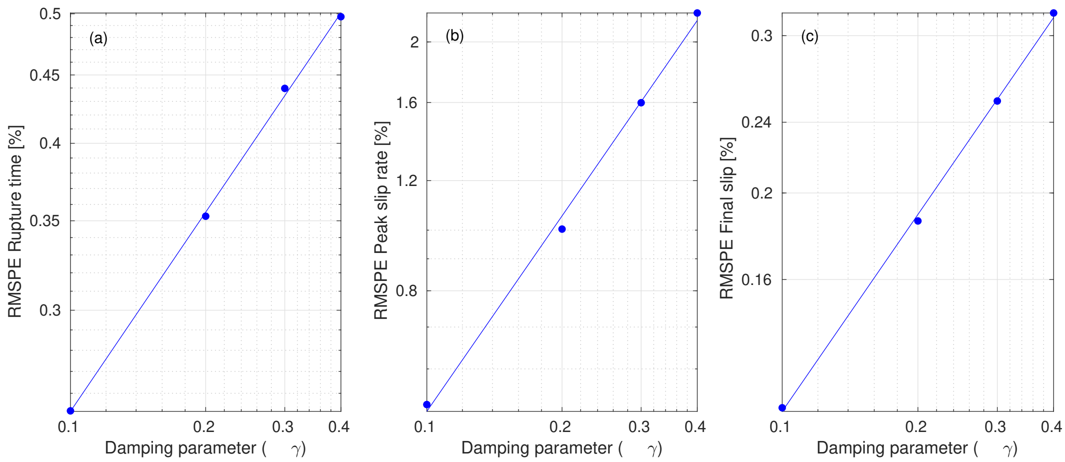

Figure 2: Convergence results of TPV104 for $\gamma = 0.1, 0.2, 0.3, 0.4$ relative to the undamped solution, $\gamma = 0.0$. The circles are the RMSPE for selected rupture features and the lines are the logarithm linear regressions. (a) RMSPE of the rupture time along the fault with convergence rate of 0.4952. (b) RMSPE of the peak slip rate considering all the on-fault stations of the benchmark with convergence rate of 1.0382. (c) RMSPE of the final slip considering all the on-fault stations of the benchmark with a convergence rate of 0.7324.

Artículo en prensa / Article in press

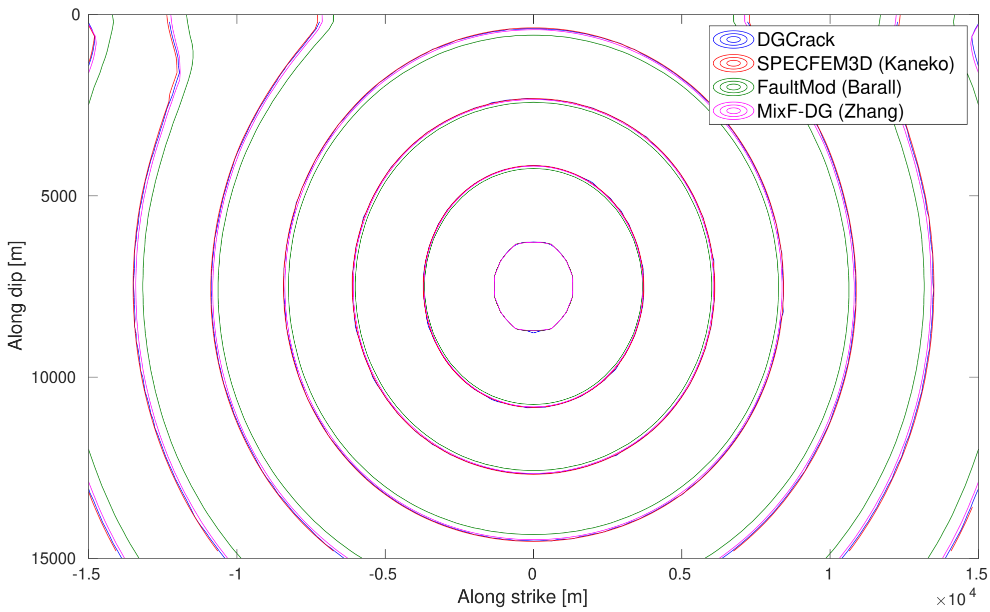

Figure 3: TPV104 Contour plots of rupture times along the fault.

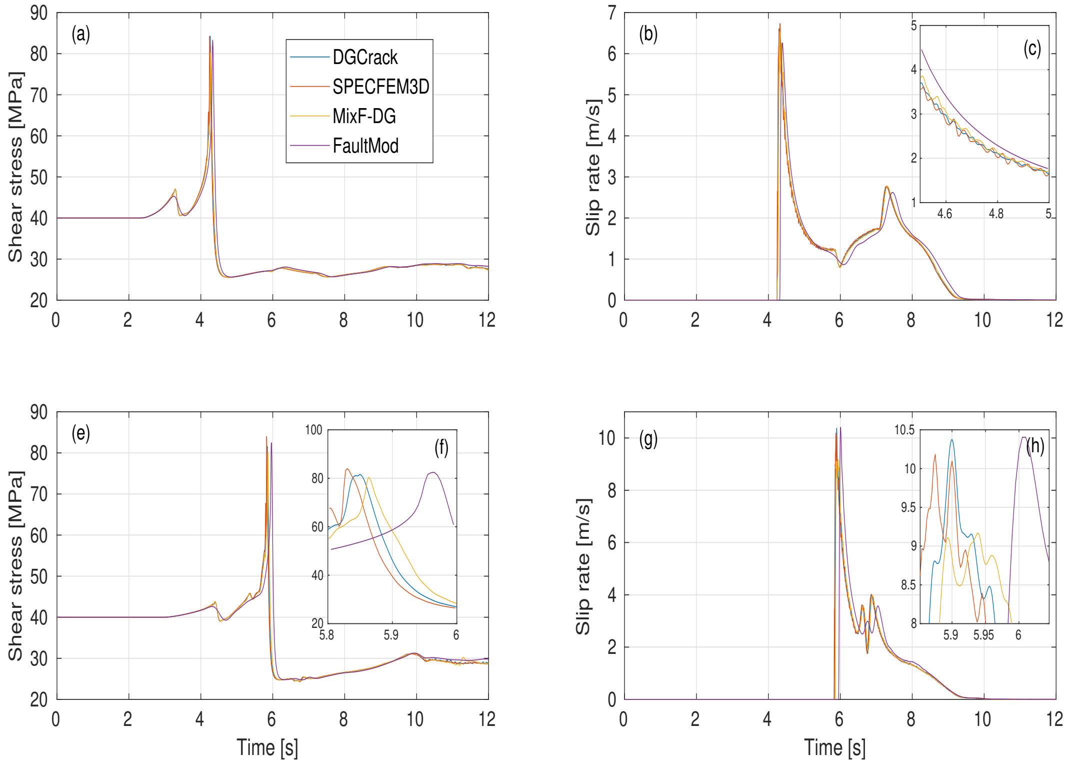

Figure 4: On-fault records for the different numerical strategies, DGCrack, SPECFEM3D, MixF-DG and FaultMod. The DOFs equivalent distance for DGCrack, MixF-DG and FaultMod is 50 m, while for SPECFEM3D is 12.5 m. Horizontal shear stress $[MPa]$ and slip rate $[m/s]$ at the fault station located 9 km along strike and 7.5 km along dip from the hypocenter, (a) and (b) respectively. (c) shows the noisest segment of the slip rate plot in (b). Horizontal shear stress $[MPa]$ and slip rate $[m/s]$ at the fault station located 12 km along strike and 3 km along dip from the hypocenter, (e) and (g) respectively. (f) and (h) are plots around the peak of the shear stress, (e), and the slip rate, (g), respectively.

Artículo en prensa / Article in press

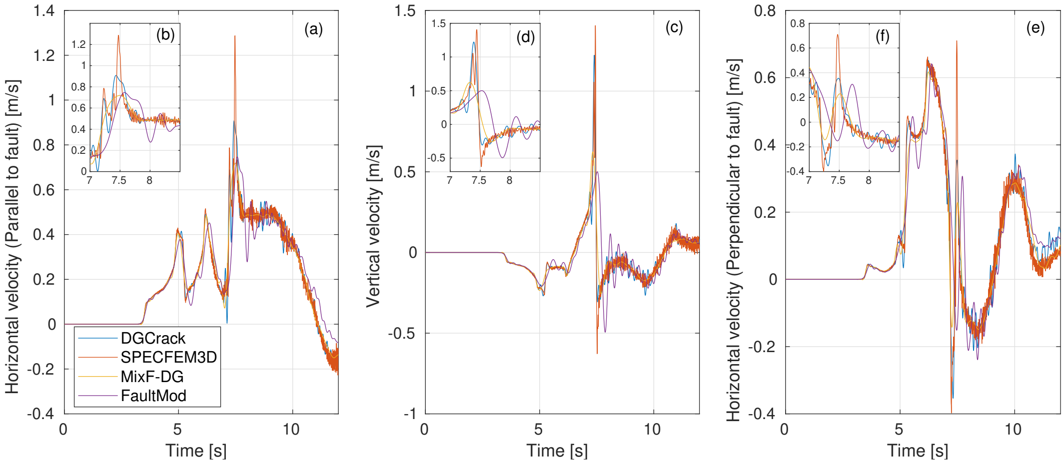

Figure 5: Free surface off-fault records at a station located 12 km along strike and 6 km perpendicular to the fault. The DOFs equivalent distance for DGCrack, MixF-DG and FaultMod is 50 m, while for SPECFEM3D is 12.5 m. (a) and (e) are the parallel and perpendicular to the fault horizontals velocity field components $[m/s]$ and (c) is the vertical velocity field component $[m/s]$. (b), (d) and (f) show the intervals with the peak values of the corresponding velocity field.

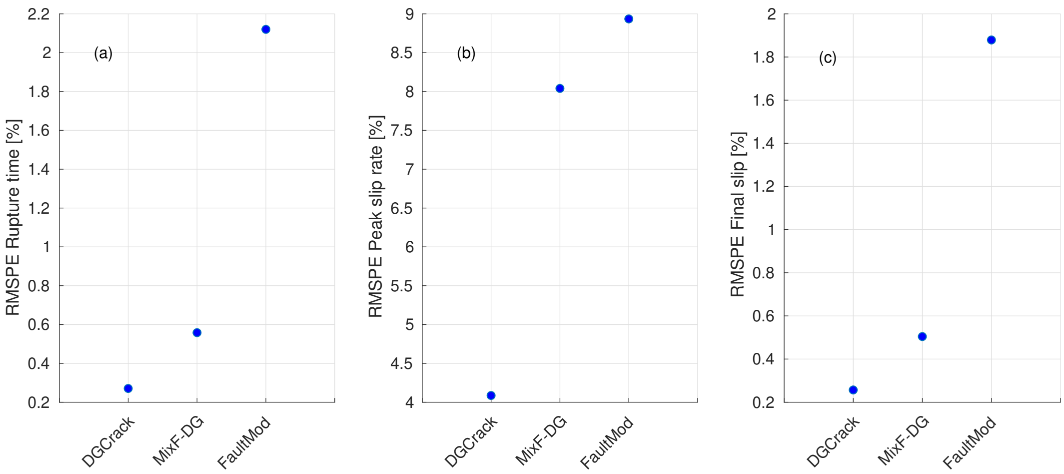

Figure 6: On-fault metrics comparison with SPECFEM3D. (a) RMSPE Rupture time [%] along the fault. (b) RMPSE Peak Slip rate [%] considering all 9 on-fault records. (c) RMPSE Final slip [%] considering all 9 on-fault records.

Artículo en prensa / Article in press

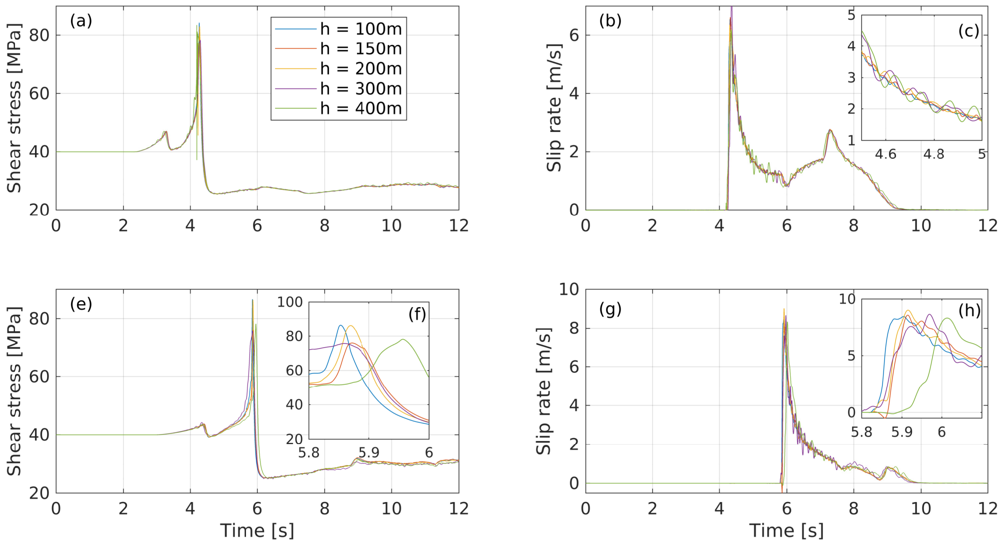

Figure 7: On-fault records for different grid sizes, $h = \{100, 150, 200, 300, 400\}\ m$. Horizontal shear stress $[MPa]$ and slip rate $[m/s]$ at the fault station located $9\ km$ along strike and $7.5\ km$ along dip from the hypocenter, (a) and (b) respectively. (c) shows the noisest segment of the slip rate plot in (b). Horizontal shear stress $[MPa]$ and slip rate $[m/s]$ at the fault station located $12\ km$ along strike and $12\ km$ along dip from the hypocenter, (e) and (g) respectively. (f) and (h) are plots around the peak of the shear shear stress, (e) and the slip rate, (g), respectively.

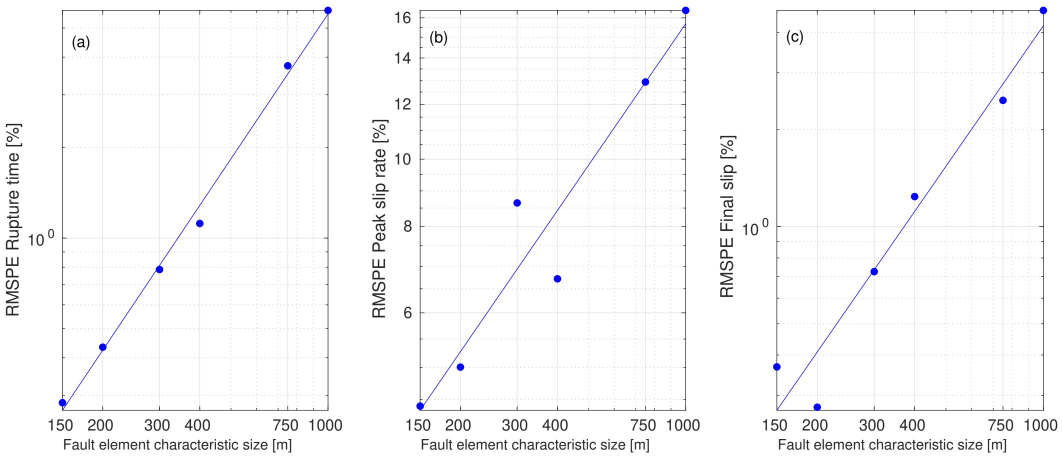

Figure 8: Convergene results of TPV104 for $h = \{150, 200, 300, 400, 700, 1000\}\ m$ relative to the finest grid size, $h = 100\ m$ with $\gamma = 0.2$. The circles are the RMPSE for selected rupture features and the lines are the logarithm linear regressions. (a) RMSPE of the rupture time along the fault with convergence rate of 1.6008. (b) RMPSE of the peak slip rate considering all the on-fault stations of the benchmark with convergence rate of 0.6774. (c) RMSPE of the final slip considering all the on-fault stations of the benchmark with a convergence rate of 1.4470.

Artículo en prensa / Article in press